Case Studies in Construction Materials 25 (2026) e06407

Contents lists available at ScienceDirect

Case Studies in Construction Materials

journal homepage: www.elsevier.com/locate/cscm

Unlocking the role of $Al(OH)_3$ in the evolution of mechanical properties of magnesium oxysulfate (MOS) cement

Kairong Jin [a,b,c,d], Huijun Xue [a,b,c,d], Zhiqi Hu [e], Hailong Wang [a,b,c,d,*], Wei Wang [f], Xiangming Zhou [g,*,*]

[a] State Key Laboratory of Water Engineering Ecology and Environment in Arid Area, Inner Mongolia Agricultural University, Hohhot, Inner Mongolia 010018, PR China
[b] College of Water Conservancy and Civil Engineering, Inner Mongolia Agricultural University, Hohhot, Inner Mongolia 010018, PR China
[c] Autonomous Region Collaborative Innovation Center for Integrated Management of Water Resources and Water Environment in the Inner Mongolia Reaches of the Yellow River, Hohhot, Inner Mongolia 010018, PR China
[d] Inner Mongolia Key Laboratory of Ecohydrology and High-Efficient Utilization of Water Resources, College of Water Conservancy and Civil Engineering, Inner Mongolia Agricultural University, Hohhot, Inner Mongolia 010018, PR China
[e] School of Civil Engineering, University of Science and Technology, Anshan, Liaoning 114051, PR China
[f] Ningxia Construction Project Quality and Safety General Station, Yinchuan, Ningxia 750021, PR China
[g] Department of Civil & Environmental Engineering, Brunel University of London, Uxbridge, Middlesex UB8 3PH, United Kingdom

ARTICLE INFO

Keywords:
Magnesium oxysulfate cement
Amorphous aluminum hydroxide
$5Mg(OH)_2{\cdot}MgSO_4{\cdot}7H_2O$ phase
Mechanical properties
Water resistance

ABSTRACT

Magnesium oxysulfate (MOS) cement is widely used in façade panels and building components, but its broader application is limited by inadequate water resistance. This study incorporated $Al(OH)_3$ into MOS cement to improve its mechanical properties and water resistance and, more importantly, to elucidate the underlying hydration-regulation mechanism. The effects of $Al(OH)_3$ were systematically investigated through mechanical testing, water immersion, phase and thermal analyses, pore structure characterisation, solid-state ^{27}Al NMR, SEM, and HR-TEM. MOS cement containing 3% $Al(OH)_3$ achieved a 28-d compressive strength of 81.6 MPa, 10.8% higher than that of the control. After 56 d of water immersion, the specimen containing 6% $Al(OH)_3$ exhibited the highest compressive strength of 59.1 MPa, representing a 12.3% improvement over the control. Mechanistically, $Al(OH)_3$ participated in the hydration process by consuming OH^- released during MgO hydration, thereby suppressing $Mg(OH)_2$ formation and regulating the content and crystal growth of the strength-bearing $5Mg(OH)_2{\cdot}MgSO_4{\cdot}7H_2O$ (5·1·7) phase. Meanwhile, amorphous aluminium hydroxide formed and became distributed within the matrix and interwoven with the 5·1·7 phase at the nanoscale. The coupled evolution of these hydration products refined the pore structure and densified the cement matrix, compensating for the reduction in 5·1·7 phase content and enhancing mechanical performance. After water immersion, the 5·1·7 phase underwent partial transformation accompanied by the formation of plate-like and flower-like basic magnesium sulfate phases. Amorphous aluminium hydroxide associated with the 5·1·7 phase mitigated water-induced deterioration, contributing to improved strength retention. These findings reveal that $Al(OH)_3$ enhances MOS cement through coupled regulation of OH^-

* Corresponding author at: State Key Laboratory of Water Engineering Ecology and Environment in Arid Area, Inner Mongolia Agricultural University, Hohhot, Inner Mongolia 010018, PR China.
** Corresponding author.
E-mail addresses: nndwhl@imau.edu.cn (H. Wang), xiangming.zhou@brunel.ac.uk (X. Zhou).

https://doi.org/10.1016/j.cscm.2026.e06407
Received 2 May 2026; Received in revised form 12 July 2026; Accepted 7 August 2026
Available online 8 August 2026

availability, hydration-product evolution, and microstructural densification, providing a mechanistic basis for designing water-resistant MOS cement.

1. Introduction

Portland cement, produced by calcining limestone at approximately 1450 °C, contributes around 8% of global anthropogenic carbon emissions and has dominated the construction industry for several decades [1]. Climate change, driven by greenhouse gas emissions such as CO_2 and CH_4, with CO_2 being the most significant contributor, has increased awareness of its environmental impact [2]. In response, low-carbon cementitious materials have attracted growing attention as potential alternatives [3–5]. Among these, MgO-based cements, including magnesium silicate cement and magnesium oxysulfate (MOS) cement, are considered promising due to their relatively low calcination temperature when producing MgO from magnesite or dolomite, resulting in reduced carbon emissions compared with Portland cement [2,6]. Within MgO-based systems, the use of MOS cement has been on the rise for manufacturing lightweight boards for decorative and fire-resistant purposes [7].

MOS cement is generally created from light-burned magnesium (LBM) combined with a magnesium sulfate solution and consists primarily of hydration phases described by $x\mathrm{Mg(OH)_2}\cdot y\mathrm{MgSO_4}\cdot z\mathrm{H_2O}$ [2]. However, the presence of excessive MgO in the matrix adversely affects the softening coefficient due to microstructural changes associated with MgO hydration, thereby limiting its practical application. To address this issue, various additives have been introduced, promoting the nucleation and generation of the 5Mg$(OH)_2\cdot MgSO_4\cdot 7\,H_2O$ (5·1·7) phase, which enhances strengths and water resistance within a certain range. The 5·1·7 phase, being more stable than metastable phases such as $3Mg(OH)_2\cdot MgSO_4\cdot 8H_2O$ (3·1·8) phase, is the predominant hydration product in the MOS cement matrix [8–11]. The presence of citric acid (CA) in cement triggers the nucleation of needle-like 5·1·7 phases, thereby reducing porosity and improving mechanical strength through better particle interconnection [2,9]. Tartaric acid slightly inhibits $Mg(OH)_2$ formation by generating a hydration film on active MgO (a-MgO), resulting in a prolonged setting time and increased strength [10]. Similarly, phosphoric acid or calcium citrate enhances the amount and coarseness of the 5·1·7 phase, refining engineering performance and softening coefficient [11]. The use of boric acid can extend hydration time, as well as enhance the content of the 5·1·7 phase, particularly in systems with high a-MgO content [12]. Moreover, additives such as ammonium citrate tribasic regulate ion concentrations (H^+ or OH^-), inhibit MgO hydration, and facilitate the growth of 5·1·7 phase, thereby reducing porosity and improving both engineering properties and water resistance [13]. The incorporation of sodium malate and trisodium citrate enhances performance by increasing gel pore content through the filling effect of the 5·1·7 phase [14,15]. Despite these improvements, the softening coefficient and volume stability of MOS cement remain strongly influenced by residual MgO, which continues to hinder its wider application [16–18]. Therefore, alternative strategies beyond conventional chemical additives are required. One promising approach involves the introduction of gel phases into MOS cement to regulate microstructure and enhance engineering performance.

Previous studies have demonstrated that incorporating ferric sulfate delays the nucleation and generation of the 5·1·7 phase, and the formation of $Fe(OH)_3$ gel contributes to a denser matrix and improved volume stability [16]. The addition of admixtures such as pulverised fuel ash or silica fume results in the creation of magnesium silicate hydrate gel, enhancing compressive strength and raising the softening coefficient to levels exceeding 0.95 [18,19]. Similarly, the inclusion of desulfurization gypsum facilitates the production of magnesium-sulfate-calcium hydrate gel, improving particle bonding and water resistance [20]. The use of hydromagnesite facilitates the generation of $MgCO_3\cdot Mg(OH)_2\cdot 3\,H_2O$, which consumes excessive MgO and enhances both mechanical properties and softening coefficient [21]. These findings highlight the effectiveness of gel-phase regulation in improving MOS cement performance.

Amorphous aluminium hydroxide is known to form under moderately alkaline conditions and can significantly influence the mechanical characteristics of aluminate-based cements [22,23]. Notably, the pore solution pH of MOS cement is generally below 12.0 [6], providing a chemical environment in which aluminium-bearing species may undergo transformation during hydration. In hydraulic cement systems, amorphous aluminium hydroxide derived from calcium aluminates contributes to improved water resistance and durability [22]. In calcium sulfoaluminate cement, increased formation of amorphous aluminium hydroxide leads to a denser matrix and enhanced performance [23–25]. Despite its recognised importance in other cementitious systems, the role of amorphous aluminium hydroxide in MOS cement remains poorly understood. $Al(OH)_3$ is amphoteric and can react under both acidic and alkaline conditions. In acidic media, it dissolves through proton-assisted reactions to release aqueous Al-bearing species, whereas under sufficiently alkaline conditions, it can interact with OH^- to form soluble aluminate species, predominantly $Al(OH)_4^-$. This amphoteric reactivity provides a specific rationale for introducing $Al(OH)_3$ into MOS cement. During MgO hydration, the evolving pore solution contains OH^- and its alkalinity is closely associated with the formation of $Mg(OH)_2$ and the $5Mg(OH)_2\cdot MgSO_4\cdot 7H_2O$ (5·1·7) phase. Therefore, $Al(OH)_3$ may participate in the hydration process by interacting with the evolving OH^- environment, thereby modifying the formation and crystalline development of hydration products and potentially promoting the formation of amorphous aluminium-bearing species. Previous studies have shown that the mechanical performance of MOS cement can be improved by regulating the formation of the 5·1·7 phase, suppressing excessive $Mg(OH)_2$ formation, introducing gel-forming components, and refining the pore structure. Building on these approaches, we further discuss the amphoteric reactivity of $Al(OH)_3$ and its potential interaction with the evolving OH^--containing pore solution generated during MgO hydration. Under sufficiently alkaline conditions, $Al(OH)_3$ can interact with OH^- to form soluble aluminate species, predominantly $Al(OH)_4^-$, thereby potentially modifying the local chemical environment governing hydration-product formation and crystalline development. On this basis, the present study investigates the effects of $Al(OH)_3$ on the mechanical properties, water resistance, hydration-product assemblage, pore structure and microstructural evolution of MOS cement. Particular attention is given to elucidating how $Al(OH)_3$ participates in hydration and

Table 1
Chemical compositions (wt%) of LBM.

Component	MgO	Al_2O_3	SiO_2	K_2O	CaO	Fe_2O_3	others
LBM	93.3%	0.42	3.57	0.02	1.73	0.54	0.42

regulates the formation and crystalline development of $Mg(OH)_2$ and the 5·1·7 phase. The findings provide new insight into the hydration-regulating role of $Al(OH)_3$ and offer a potential strategy for enhancing the mechanical performance and water resistance of MOS cement.

2. Materials and Methods

2.1. Raw materials

Sourced from Haicheng in Liaoning Province, China, light-burned magnesia (LBM) was utilised in this paper and produced by the calcination of magnesite. Using hydration methods [6], the active MgO (a-MgO) proportion in LBM was identified to be 63.8%. Presented in Table 1 is the chemical composition of LBM. $Al(OH)_3$ and citric acid (CA) were sourced from Yifeng Co., Ltd. (Ningxia, China), each with a purity higher than 99.8%. Citric acid (CA) was used at a dosage of 0.5% based on the weight of LBM. Acquired from Nanfeng Co., Ltd. in Shanxi, China, $MgSO_4·7H_2O$ has a purity exceeding 99.9%.

Figs. 1 and 2 present the XRD patterns, TG-DTG curves, and SEM image of $Al(OH)_3$. The measured mass loss of $Al(OH)_3$ was 34.5%, corresponding to the characteristic decomposition of gibbsite [26]. As shown in Figs. 1 and 2, the $Al(OH)_3$ used in the study exhibited good crystallinity and was predominantly composed of gibbsite.

2.2. Specimen preparation

A control specimen, denoted as MOSAH1, was prepared without $Al(OH)_3$. For the modified specimens, $Al(OH)_3$ was incorporated as a percentage of LBM mass, with dosages ranging from 3 wt% to 12 wt% at 3 wt% intervals. The specimens were labelled MOSAH2 to MOSAH5, respectively. Molar ratio of $MgSO_4$ to a-MgO was established at 0.125, with the H_2O to $MgSO_4·7H_2O$ ratio maintained at 0.077. To prepare the $MgSO_4$ solution, $MgSO_4·7H_2O$ crystals were dissolved in distilled water and allowed to sit at room temperature for 24 h before using it. The predetermined amounts of LBM and $Al(OH)_3$ were first placed in the bowl of a standard planetary mixer. The selected molar proportions were based primarily on previous systematic studies of the effects of $MgO/MgSO_4$ and $MgSO_4/H_2O$ ratios on the hydration and pore-structure evolution of MOS cement. Tang et al. [26]. reported that, although variation in the $MgO/MgSO_4$ ratio did not substantially affect the crystallinity of the principal hydration products, the mixture proportions significantly influenced hydration kinetics and pore structure. In particular, an $MgO:MgSO_4:H_2O$ molar ratio of 8:1:20 resulted in relatively lower porosity and pore volume together with higher hydration heat release, indicating a denser microstructure and more rapid hydration development [6,9,26]. This ratio has also been adopted in previous studies of modified MOS cement systems, including MOS cement incorporating fly ash [27]. Therefore, the 8:1:20 ratio was selected as a well-established reference formulation with favourable hydration and microstructural characteristics, allowing the specific influence of $Al(OH)_3$ on hydration, phase evolution, mechanical properties, and water resistance to be systematically evaluated. The $MgSO_4$ solution was then gradually added over 60 s during mixing. The mixer was subsequently paused for 60 s to manually scrape material adhering to the sides and bottom of the bowl to ensure homogeneity, followed by a further 180 s of mixing. Immediately after mixing, the fresh MOS paste was cast into pre-assembled and lubricated steel moulds ($40 \times 40 \times 160$ mm^3). The filled moulds were then transferred to a curing chamber and maintained at room temperature for the first 24 h. After demolding, the samples were kept for curing at a constant 20 ± 1 °C and $60 \pm 5\%$ relative humidity. After 28 days, certain samples were placed in water to assess their resistance to moisture. Distilled water was used for the water-immersion tests to minimise interference from external ions and to isolate the intrinsic water-resistance behaviour of MOS cement. In particular, the absence of externally introduced Ca^{2+} minimised the potential formation of gypsum ($CaSO_4·2H_2O$) through reaction with SO_4^{2-} released from the cement matrix, thereby avoiding additional phase transformations that could interfere with the evaluation of the stability of the 5·1·7 phase. The pH of the distilled water was measured as 7.1 using a PHS-3C pH meter (INESA, Shanghai, China). For the pH measurements of MOS cement, 1.0 g of powdered sample with a particle size below 75 μm was dispersed in 10 mL of ultrapure water. The suspension was stirred for approximately 24 h and subsequently filtered through a 200 nm membrane. The pH of the resulting filtrate was measured using a PHS-3C pH meter (INESA, Shanghai, China).

2.3. Experiment methods

The evaluation of the strengths of MOS cement was carried out following the GB/T 17671–2021. For this assessment, a YES−2000 electronic servo-controlled apparatus was employed, applying a load at 1.6 kN/s. The strength of each sample was calculated as the average value obtained from six replicate measurements. Independent-samples *t*-tests were performed for intergroup comparisons of compressive strength. Employing a DX−2700BH diffractometer, phase identification was completed through X-ray diffraction (XRD). Experimental data were captured within a 2-theta range of 5° to 85°, utilising a step size of 0.02°, as well as a counting time of 0.03 s

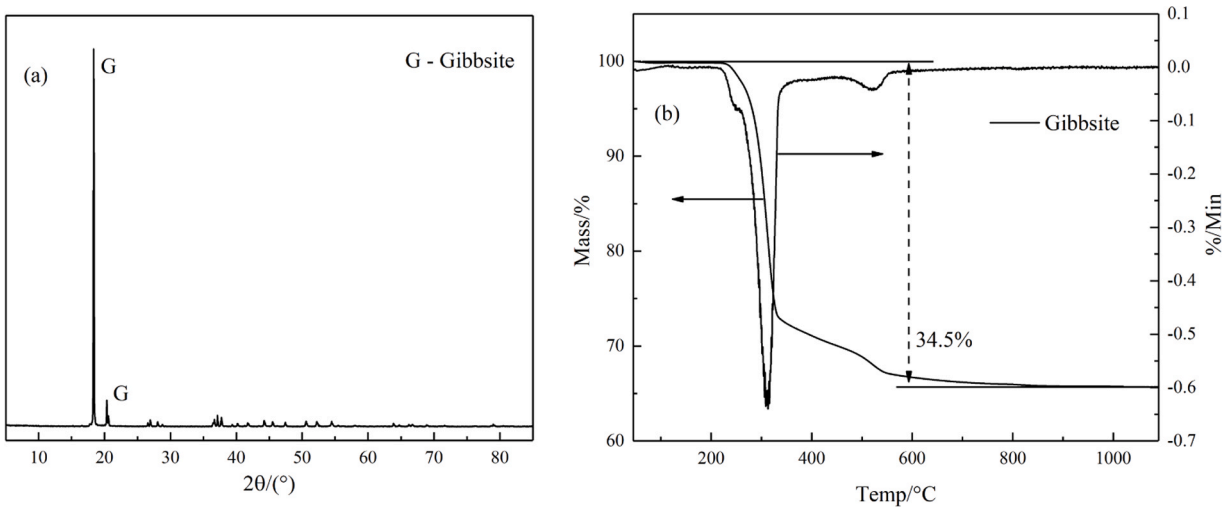

Fig. 1. XRD patterns and TG-DTG curves of $Al(OH)_3$: (a) XRD patterns; (b) TG-DTG curves.

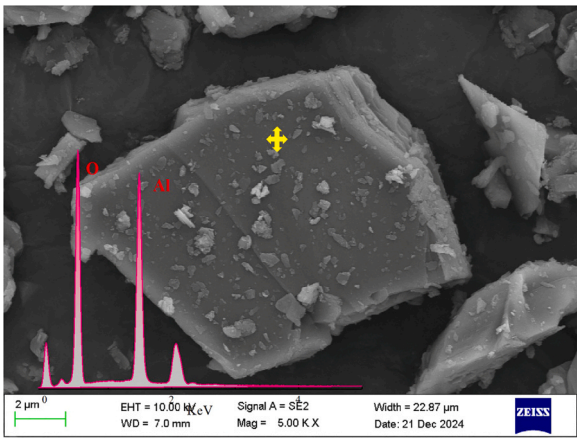

Fig. 2. SEM image of $Al(OH)_3$.

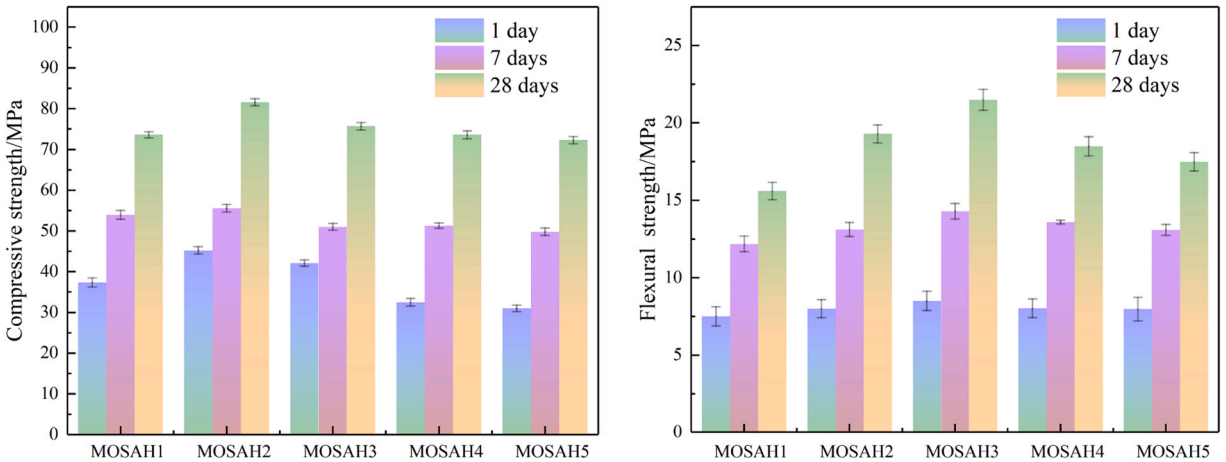

Fig. 3. Strengths of MOS cement subjected to curing over varying time periods: (a) compressive strength; (b) flexural strength.

for every increment. In addition, a Bruker 400 M spectrometer was used to conduct solid-state ^{27}Al nuclear magnetic resonance (NMR) spectroscopy, which focused on analysing the atomic-level chemical environment.

Microstructure and elemental distribution were examined using scanning electron microscopy (SEM, GeminiSEM 300) combined with energy-dispersive X-ray spectroscopy (EDS). HR-TEM (Talos 200S) provided additional insights into crystallographic characteristics, such as lattice spacing. Thermal characteristics were evaluated by employing simultaneous thermogravimetric analysis and differential scanning calorimetry (TG-DSC) with an STA449F5 instrument. In a nitrogen atmosphere, measurements were taken while gradually increasing the temperature from 45 to 1100 °C at a rate of 5 °C/min. FT-IR spectra were collected using a Nicolet iS50 spectrometer over the wavenumber range of 400–4000 cm^{-1} using the KBr pellet method. Finally, MIP was employed by a Micromeritics Autopore V 9605 device to assess the pore structure of hardened pastes.

3. Results

3.1. Strengths

In Fig. 3, the strengths of $Al(OH)_3$-modified MOS cement are displayed. Incorporating $Al(OH)_3$, as illustrated in Fig. 3(a), resulted in a significant enhancement of the compressive strength of MOS cement. After 3 days of curing, MOSAH2 reached the peak compressive strength of 45.3 MPa, while MOSAH5 recorded the lowest value of 31.1 MPa. After 28 days of curing, the compressive strength of MOSAH2 reached 81.6 MPa, which was the highest among all specimens and 10.8% greater than that of MOSAH1. These observations imply that the incorporation of an appropriate amount of $Al(OH)_3$ enhanced the compressive strength of MOS cement. Fig. 3(b) demonstrates the effects of $Al(OH)_3$ on the cement's flexural strength. With greater $Al(OH)_3$ addition, the flexural strength exhibited an initial upward trend followed by a downward turn. After the specimens had cured for 28 days, MOSAH3 showcased the maximum flexural strength of 21.5 MPa, which signifies a 37.8% rise in comparison to MOSAH1, while MOSAH5 reported a flexural strength of 17.5 MPa. The results confirm that flexural strength in MOS cement benefits most from an optimal $Al(OH)_3$ addition.

3.2. Hydration products

The XRD patterns displayed in Fig. 4 represent MOS cement containing $Al(OH)_3$ that has undergone air curing for varying time periods. Distinct diffraction peaks of gibbsite were observed, indicating that gibbsite within the MOS cement matrix was not entirely involved in the hydration reaction. In Fig. 4(a), the peak at $2\theta = 37.97°$, identified as the (011) lattice plane of $Mg(OH)_2$, was barely visible, likely owing to the comparatively low crystallinity of $Mg(OH)_2$. Inclusion of $Al(OH)_3$ did not enhance the creation of $Mg(OH)_2$, even after 3 days of hydration. At the end of the 28-day curing regime, the intensity of the $Mg(OH)_2$ diffraction peak at $2\theta = 37.97°$ decreased with increasing $Al(OH)_3$ content. Besides, the crystal dimensions of $Mg(OH)_2$ along the (011) plane were calculated using the Scherrer equation, which utilised a constant of 0.943 and an X-ray wavelength of 0.154056 nm [26–28]. Having undergone 28 days of curing, the crystal sizes of $Mg(OH)_2$ in MOSAH1, MOSAH2, MOSAH3, and MOSAH5 were 37.3, 31.9, 30.8, and 27.9 nm, respectively. Because the generation of $Mg(OH)_2$ primarily relies on the MgO's hydration, and the higher levels and larger sizes of $Mg(OH)_2$ are usually detrimental to the engineering characteristics of MOS cement [29], these findings suggest that $Al(OH)_3$ suppressed the development of $Mg(OH)_2$ crystals, thus affecting the mechanical properties of MOS cement. The sizes of the crystals in the 5·1·7 phase at the (222) plane were determined for MOSAH1, MOSAH2, MOSAH3, and MOSAH5 after three days of curing, with measurements recorded at 37.9 nm, 43.6 nm, 44.5 nm, and 46.3 nm, respectively. After 28 days of curing, the corresponding values were

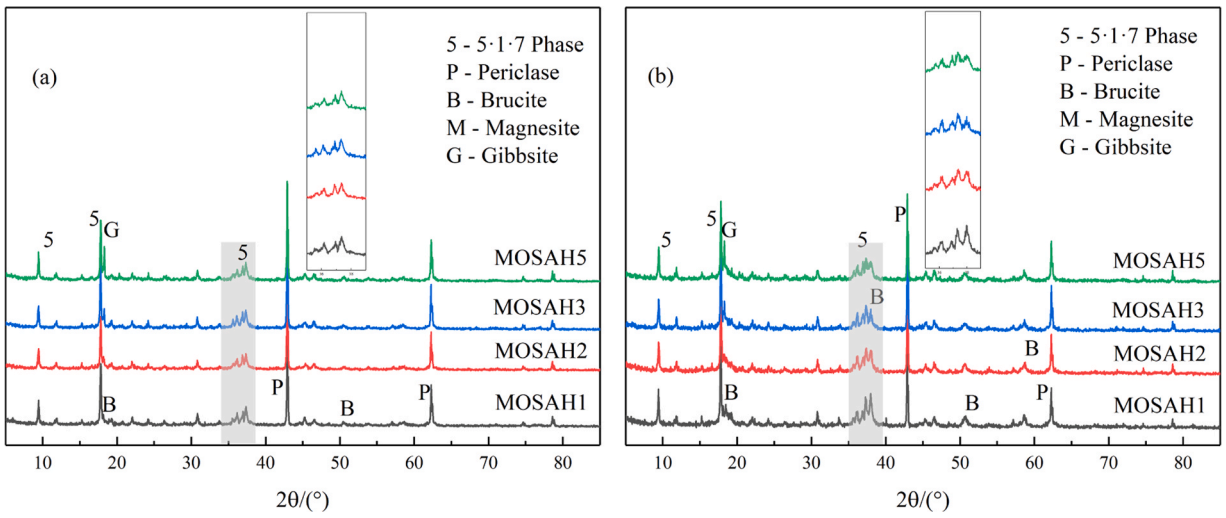

Fig. 4. XRD spectra of MOS cement subjected to curing for (a) 3 days and (b) 28 days.

44.6, 44.5, 44.8, and 40.2 nm, respectively. The data reveal that the addition of $Al(OH)_3$ accelerated 5·1·7 crystal growth during the initial hydration period of MOS cement.

The TG-DTG profiles of MOS cement after diverse curing periods are provided in Fig. 5. Reactions (1) to (2) describe the decomposition of the 5·1·7 phase at different temperatures [30,31]. The DTG curves exhibited a notable shift around 395 °C, which is ascribed to $Mg(OH)_2$ decomposition.

$$5Mg(OH)_2{\cdot}MgSO_4{\cdot}7H_2O \rightarrow 5Mg(OH)_2{\cdot}MgSO_4 + 7H_2O \sim 200\ ^\circ C \quad (1)$$

$$Mg(OH)_2{\cdot}MgSO_4 \rightarrow 5MgO + MgSO_4 + H_2O \sim 420\ ^\circ C \quad (2)$$

From the TG data, the loss in mass recorded for the $Al(OH)_3$-modified MOS cement was reduced relative to the plain control, pointing to a certain inhibitory effect of $Al(OH)_3$ on hydration product development. Within the 45–200 °C region, variations in the DTG profiles point to a diminished 5·1·7 phase content in cement incorporating $Al(OH)_3$. Interpretation is also supported by the change in the DTG peaks around 420 °C. Thus, $Al(OH)_3$ inhibited the generation of the 5·1·7 phase. Besides, the decomposition temperature of a crystal is positively related to its crystallinity [32]. As shown in Fig. 5(a), the peak changes associated with the crystal water loss from the 5·1·7 phase suggested that, after 3 days of curing, the crystallinity of the 5·1·7 phase in the control specimen was relatively low. As shown in Fig. 5(b), the peaks associated with 5·1·7 phase decomposition almost overlapped after 28 days of curing, implying similar crystallinity levels across samples, in agreement with the findings in Fig. 4. The data imply that $Al(OH)_3$ modulated the crystalline development of the 5·1·7 phase during curing. Alterations in the DTG curves at approximately 395 °C, resulting from $Mg(OH)_2$ decomposition, revealed a decreased $Mg(OH)_2$ proportion in MOS cement with $Al(OH)_3$ addition. Furthermore, the decomposition peaks of $Mg(OH)_2$ shifted to lower temperatures in the $Al(OH)_3$-modified specimens (Fig. 5(b)), indicating a lower crystallinity, in agreement with the calculated results depicted in Fig. 4(b). Therefore, $Al(OH)_3$ incorporation hindered the nucleation and development of $Mg(OH)_2$ within the MOS cement matrix.

Fig. 5 also shows the variation in mass loss of MOS cement within the temperature range of 249–302 °C after curing for different periods. When comparing Figs. 5(a) and 5(b), the mass loss difference for the control specimen in this temperature range was 26.5%, whereas the corresponding values for the $Al(OH)_3$-containing specimens did not follow the same trend. In particular, the mass loss differences for MOSAH2 and MOSAH5 were 5.6% and 6.2%, respectively, which were relatively close. Although the additional contribution of $Al(OH)_3$ to mass loss should be considered, the observed changes in mass loss difference did not correspond directly to the mix proportions. These results suggest that $Al(OH)_3$ may have undergone phase transformation during curing, thereby reducing the mass loss of cement in this temperature region.

3.3. FTIR

The FTIR spectra obtained from MOS cement samples with different $Al(OH)_3$ levels after 28 days of curing are shown in Fig. 6. The signals observed at 3645 and 3712 cm^{-1} were attributed to the stretching vibrations of MgO–H bonds in $Mg(OH)_2$ [28,30]. The $\upsilon_1(SO_4)$ and $\upsilon_3(SO_4)$ vibrations produced peaks at 990 and 1109 cm^{-1} , respectively. O–H bending and stretching vibrations in water gave rise to the bands at 1651 and 3400 cm^{-1} , and the feature at 1443 cm^{-1} stemmed from O–C–O stretching in CO_3^{2-}. Signals observed at 568 and 3525 cm^{-1} were relevant to Al–O and O–H stretching modes, respectively, characteristic of AlO_6 octahedral units and gibbsite [33–35]. O-H stretching vibrations associated with AlO_6 octahedral coordination or AlO_4 tetrahedral coordination can also give rise to peaks at 3656, 3470 or 3553 cm^{-1}[34]. The pronounced broadening of the peak at 3645 cm^{-1} in the presence of $Al(OH)_3$ suggests that AlO_4 tetrahedral coordination may have been present to a certain extent. However, distinct peaks attributed to AlO_4 or AlO_5 were not observed, which may be due to the relatively lower content of amorphous aluminium hydroxide.

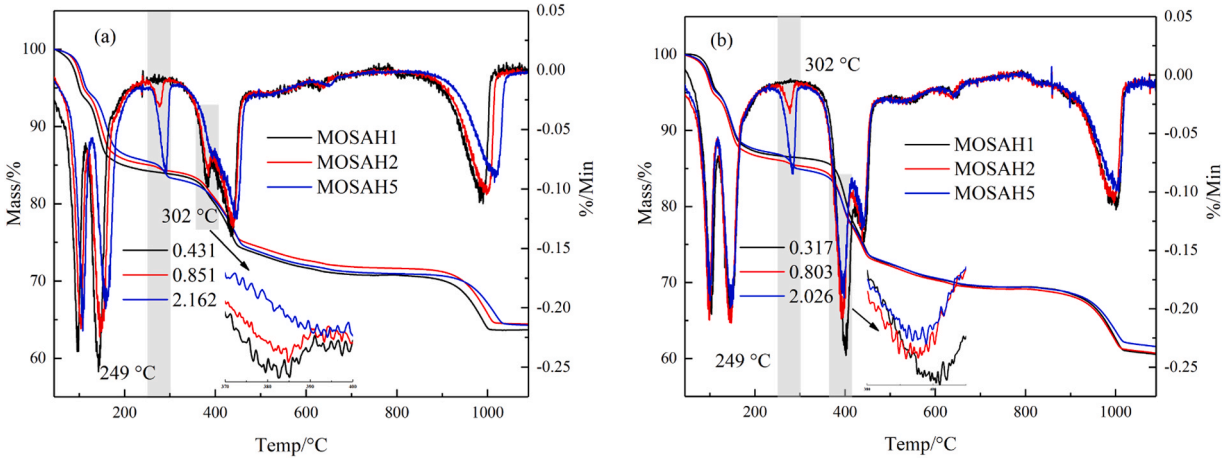

Fig. 5. TG-DTG curves of MOS cement: (a) 3 days; (b) 28 days.

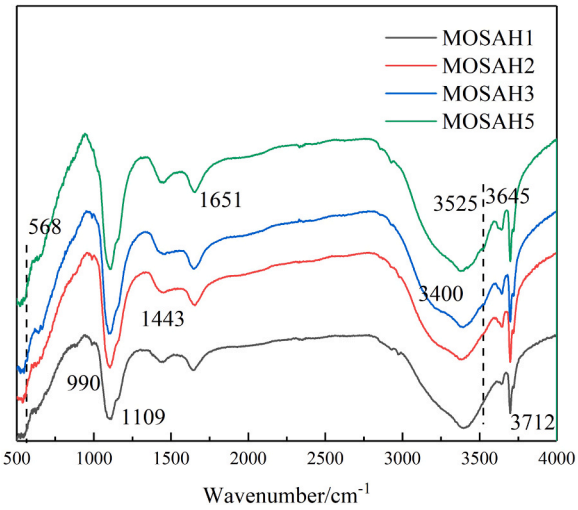

Fig. 6. FTIR spectra of MOS cement cured for 28 days.

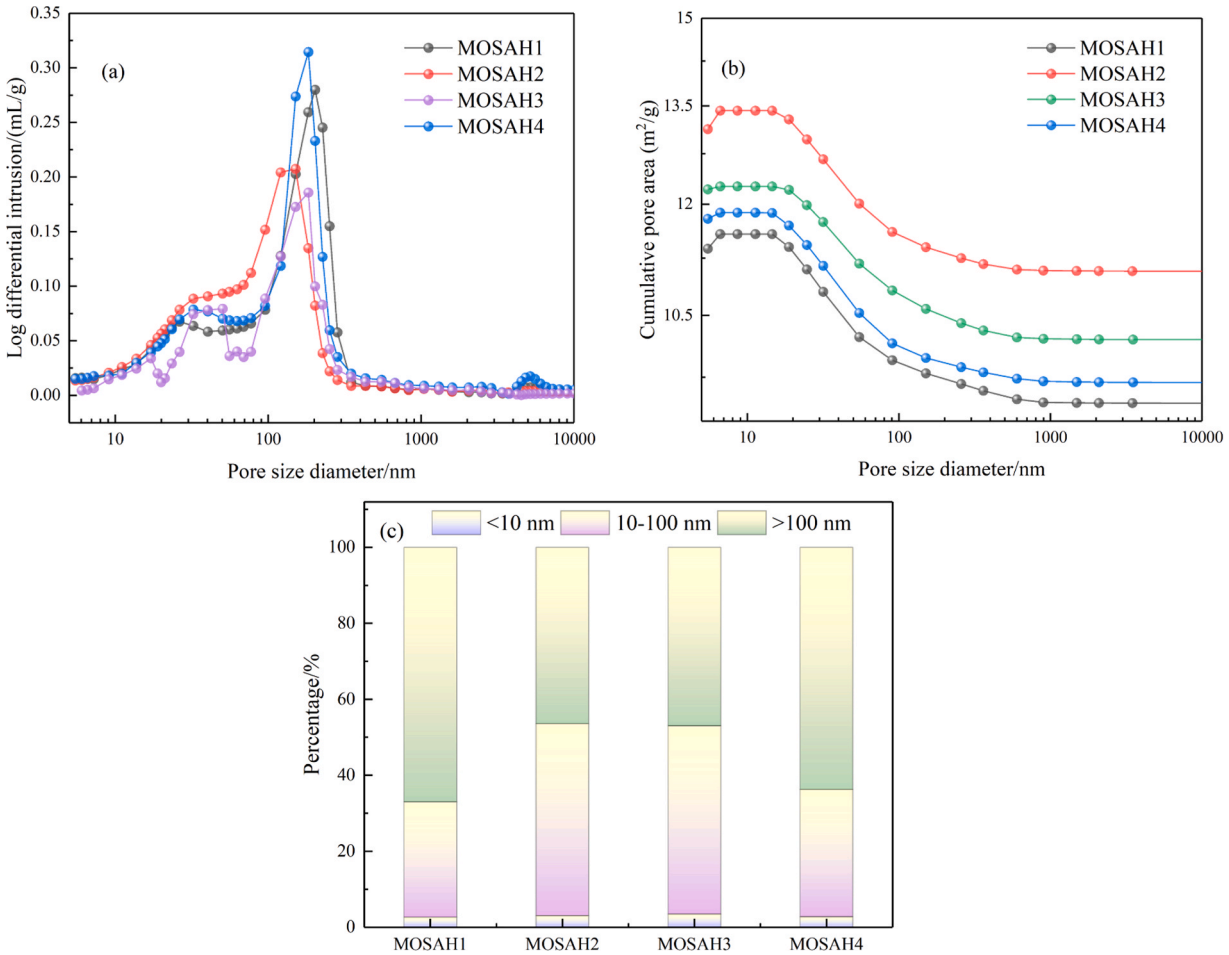

Fig. 7. MOS cement's pore characteristics: (a) pore size distribution; (b) pore area; (c) proportion of pores across different size ranges.

3.4. Pore characteristics

The pore characteristics of MOS cement cured for 28 days are shown in Fig. 7. The porosity values of MOSAH1, MOSAH2, and MOSAH4 was 29.9%, 27.8%, and 29.4%, respectively, while the corresponding average pore sizes were 70.46, 54.95, and 66.49 nm, and median pore sizes were 180.71, 112.60, and 161.50 nm, respectively. Among these specimens, MOSAH2 exhibited the lowest porosity and the smallest average and median pore sizes. The results point to a positive contribution of $Al(OH)_3$ toward a denser matrix structure in MOS cement. Pores under 10 nm accounted for 2.65%, 3.06%, and 2.74% in MOSAH1, MOSAH2, and MOSAH3, respectively, offering an indirect measure of the gel phase present. This is also consistent with variation in pore areas, as gels generally exhibit a relatively large surface area. With large-pore (>100 nm) fractions of 66.96%, 46.39%, and 63.68% for MOSAH1, MOSAH2, and MOSAH3, it is evident that $Al(OH)_3$ curtailed the presence of such pores in the MOS cement matrix. Since pores under 10 nm tend to favour the strength performance of MOS cement, in contrast to the adverse effects of pores exceeding 100 nm [28,36], the data imply that $Al(OH)_3$ upgraded the pore system and encouraged matrix densification, which in turn boosted the mechanical strength. While MOSAH3 possessed marginally lower porosity than MOSAH2, it exhibited the largest volume of gel pores smaller than 10 nm. This structural characteristic accounted for the improved water resistance of MOSAH3 to a certain extent.

3.5. NMR

Fig. 8 presents the ^{27}Al NMR spectra of MOSAH3 after curing for different periods. AlO_6 octahedral coordination, AlO_5 pentahedral coordination, and AlO_4 tetrahedral coordination are generally assigned to chemical shifts of approximately 10, 35, and 65 ppm, respectively [37]. The weak signals corresponding to AlO_5 pentahedral coordination and AlO_4 tetrahedral coordination help explain the absence of prominent related peaks in Fig. 6. In cement-based materials, AlO_6 octahedral coordination is generally associated with AFt, AFm, or well-crystallised aluminium hydroxide, whereas the peaks at approximately 35 and 65 ppm are characteristic of amorphous aluminium hydroxide [37]. The peak intensity at approximately 10 ppm for MOSAH3 before water immersion was higher than that after water immersion, indicating a higher content of well-crystallised aluminium hydroxide before immersion. Thus, water immersion altered the content of well-crystallised aluminium hydroxide in the MOS cement matrix. Following 56 days of water immersion curing, the peaks at approximately 35 and 65 ppm, assigned to amorphous aluminium hydroxide, became weaker, indicating a change in its content after immersion.

3.6. Microscopic morphology

The morphological features of MOS cement at different $Al(OH)_3$ addition levels are shown via SEM in Fig. 9. The needle-like crystals observed in the MOSAH1 matrix (Fig. 9(a)), which were identified as the 5·1·7 phase, showed an absence of detectable Al. In Fig. 9(b), the 5·1·7 phase on the matrix surface was observed, indicating that this phase developed not only within the pores but also on exposed surfaces. In the MOSAH3 matrix, an Al atomic content of 8.38% was detected on the surface of 5·1·7 crystals grown on the matrix surface (Fig. 9(b)), which is sufficiently high to be considered significant. Based on the crystal morphology and EDS results, the detected phase was not $Al(OH)_3$ itself, suggesting that Al species was likely present in the form of amorphous aluminium hydroxide adsorbed on the surface of the 5·1·7 crystals. A distinct enrichment of Al was also observed on the surface of the MOSAH3 matrix (Fig. 9

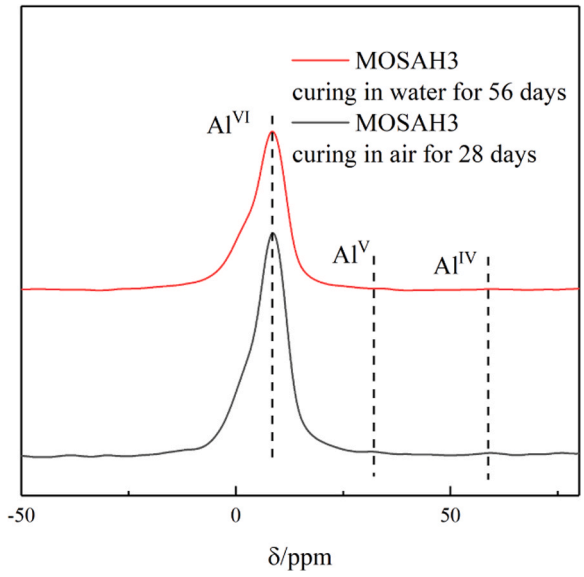

Fig. 8. ^{27}Al NMR spectra of MOSAH3 collected after air curing for 28 days and after immersion in water for a further 56 days, respectively.

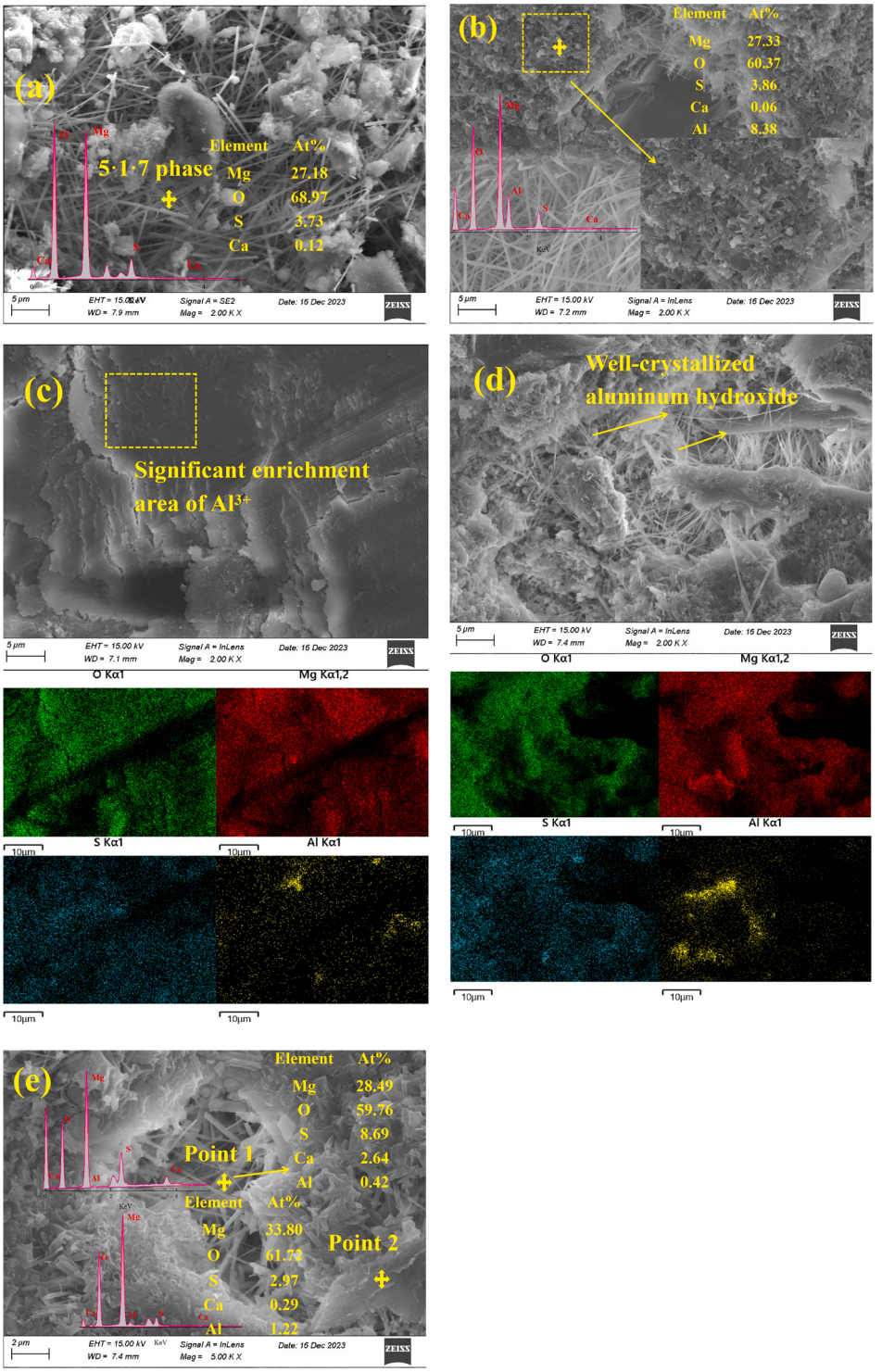

Fig. 9. SEM images of MOS cement after 28 days of curing: (a) MOSAH1; (b), (c) MOSAH3; and (d), (e) MOSAH5.

(c)), where no obvious crystalline morphology was identified, which differed from the feature shown in Fig. 9(d). In Fig. 9(e), comparison of the EDS results at Point 1 and Point 2 also confirmed the presence of Al on the surface of the MOSAH5 matrix. These findings further confirm that the features seen in Fig. 9(b) and Fig. 9(c) were systematic rather than incidental, consistent with the NMR results of Fig. 8. Thus, the addition of $Al(OH)_3$ promoted amorphous aluminium hydroxide formation and contributed positively to the strength's performance of cement.

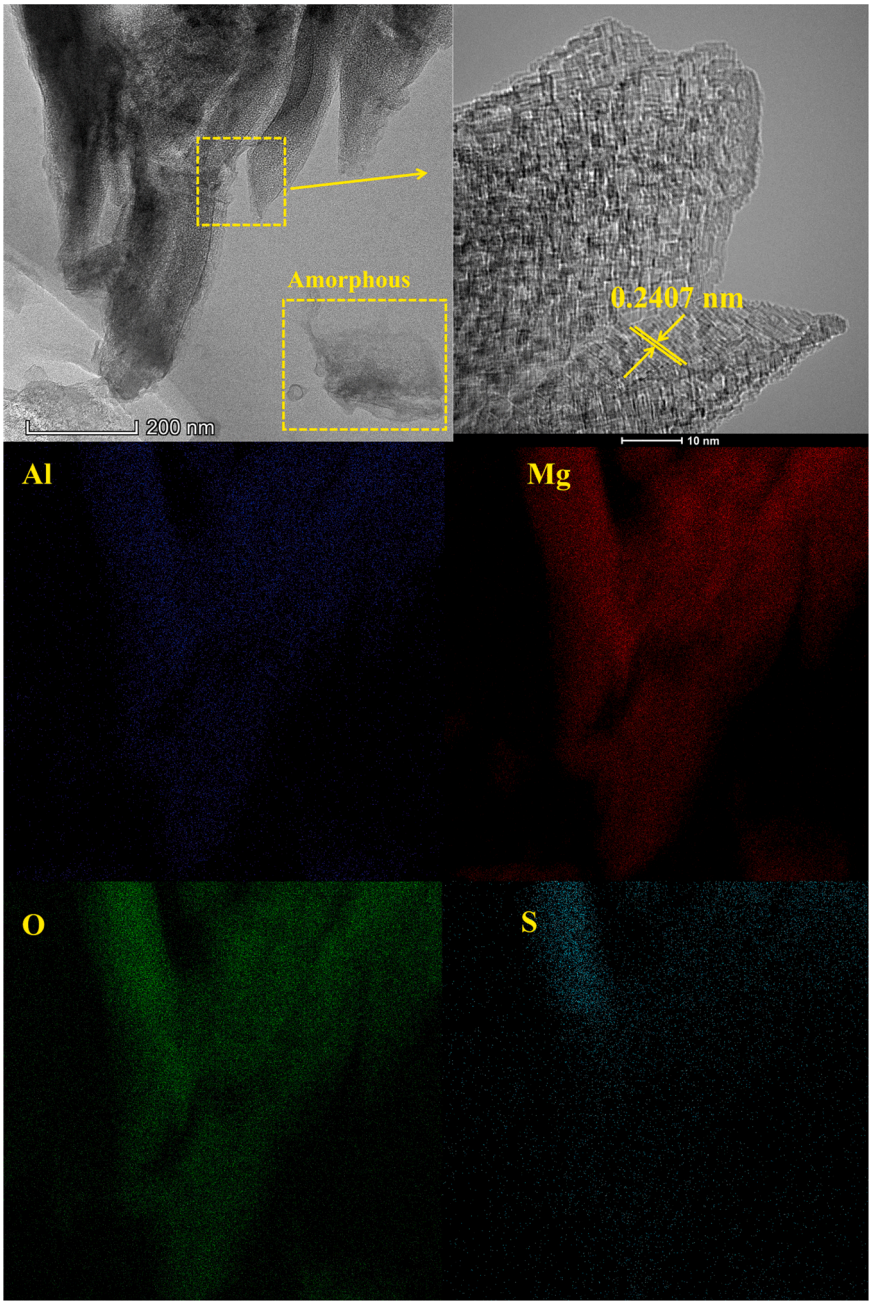

Fig. 10. HR-TEM images of MOSAH3.

Figs. 10 and S1 provide an HR-TEM view of MOSAH3 cured for 28 days under ambient conditions. Elemental mapping revealed that the observed crystal corresponded to the 5·1·7 phase and simultaneously showed significant Al enrichment. Fig. 10 reveals a d-spacing of 0.2407 nm for the crystal, which aligns with the (222) crystallographic plane of the 5·1·7 phase noticed at $2\theta = 37.33^{\circ}$. This further confirms that the observed crystal was the 5·1·7 phase. At the same time, the observed 5·1·7 crystal exhibited a layered structure composed of numerous smaller crystals, and part of its surface was covered by amorphous material. In addition, a distinct amorphous region enriched in Al was identified in Fig. 10. Although this amorphous phase cannot be conclusively identified as amorphous aluminium hydroxide, it nevertheless provides supporting evidence for its presence.

3.7. Water resistance

As shown in Figs. 11(a) and S3, the compressive strength of MOS cement varied with water immersion duration; Fig. 11(b) displays the corresponding TG-DTG curves after 56 days of water curing. After water curing, the compressive strength of all MOS cement

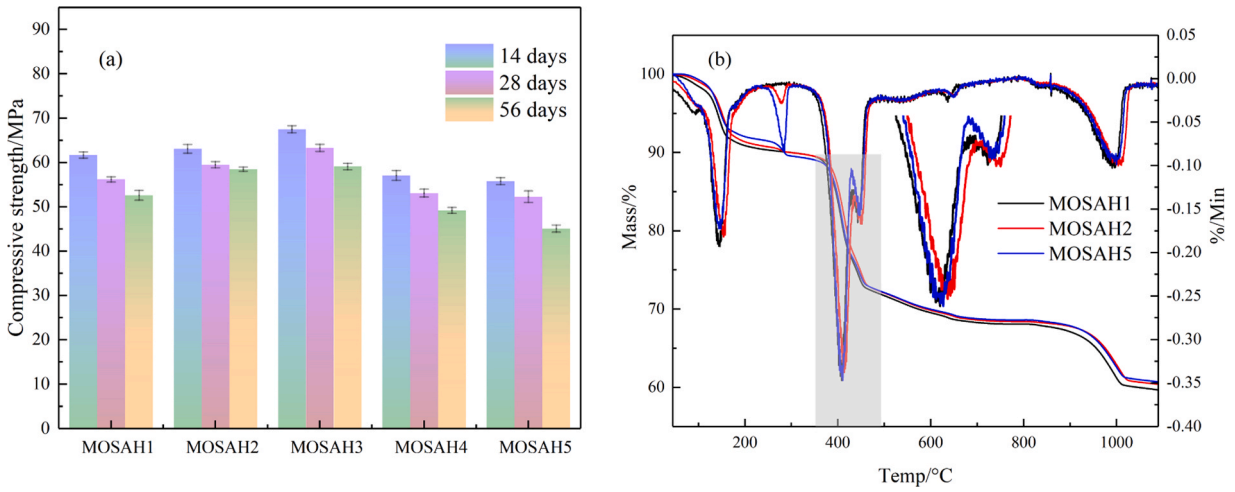

Fig. 11. TG-DTG curves and compressive strength of MOS cement after water immersion.

specimens decreased to varying degrees. With greater $Al(OH)_3$ addition, the immersed compressive strength rose to a maximum and then fell. After 56 days of water curing, the highest strength of 59.1 MPa was observed in MOSAH3, exceeding the reference specimen by 12.3%, in contrast to MOSAH5, which attained only 45.1 MPa. These results indicate that an appropriate dosage of $Al(OH)_3$ had a beneficial effect on the compressive strength of MOS cement. According to TG measurements taken after 56 days of water curing, MOSAH1 showed a greater mass loss than both MOSAH2 and MOSAH5, reflecting a more substantial quantity of hydration products formed in its matrix. Around 420 °C, the degradation peaks of $5Mg(OH)_2{\cdot}MgSO_4$ induced a displacement in the DTG traces, with the $Al(OH)_3$-modified specimens exhibiting a minor drift to elevated temperatures compared with the reference. This suggests that the crystal size or crystallinity of $5Mg(OH)_2{\cdot}MgSO_4$ in MOS cement containing $Al(OH)_3$ was greater than that in the control specimen. Similarly, the DTG peaks in the temperature range of 45–200 °C shifted slightly to higher temperatures, particularly for MOSAH5. This shift, attributed to crystal water loss from the 5·1·7 phase during heating, is consistent with the phenomenon observed around 420 °C. These changes in the DTG curves agree with the observations in Fig. 5, suggesting that the 5·1·7 phase retained relatively larger crystal size after immersion, which contributed to the retention of compressive strength.

The differences in the performance of MOS cement at varying $Al(OH)_3$ dosages were closely associated with the evolution of hydration products and microstructure. The mechanical properties of MOS cement were primarily governed by the coupled contributions of the strength-bearing 5·1·7 phase and amorphous aluminium hydroxide. However, the contents of these two products did not evolve synchronously because of their distinct formation mechanisms. Although both processes were closely related to OH^- availability, the formation of amorphous aluminium hydroxide involved the consumption of OH^- through the participation of $Al(OH)_3$ in the hydration process. In contrast, the formation of the 5·1·7 phase involved the self-assembly of Mg^{2+}, OH^-, and SO_4^{2-} species under the complexation effect of CA. Consequently, increasing the $Al(OH)_3$ dosage altered the balance between 5·1·7 phase formation and amorphous aluminium hydroxide generation, resulting in different optimum dosages for compressive strength, flexural strength, and water resistance. The variations in the 5·1·7 phase content were supported by the DTG results (Figs. 5 and 11), while the pore structure results (Fig. 7) further demonstrated that $Al(OH)_3$ modified matrix compactness and pore-size distribution. Therefore, the dosage-dependent mechanical response of MOS cement arose from the coupled evolution of hydration products and pore structure rather than from changes in a single phase.

Compressive strength is particularly sensitive to matrix compactness, load-bearing phase assemblage, and larger pore defects. At a relatively low $Al(OH)_3$ dosage (3%), the balance among suppression of $Mg(OH)_2$ growth, regulation of the 5·1·7 phase, formation of amorphous aluminium-bearing species, and pore refinement was most favourable for compressive load bearing, resulting in the highest compressive strength. In contrast, flexural strength is more sensitive to crack initiation, crack propagation, and interfacial continuity. A moderately higher $Al(OH)_3$ dosage (6%) may promote a greater amount and broader distribution of amorphous aluminium-bearing species associated with the matrix and 5·1·7 phase, thereby improving stress transfer and resistance to crack propagation despite changes in the amount of the crystalline 5·1·7 phase. Similarly, water resistance depends not only on initial matrix strength but also on resistance to water ingress, residual MgO hydration, and destabilisation of the 5·1·7 phase during immersion. The denser microstructure and increased contribution of amorphous aluminium-bearing species at 6% $Al(OH)_3$ therefore provided a more favourable balance for strength retention under water exposure. Accordingly, the different optimum dosages reflect the distinct sensitivities of compressive strength, flexural strength, and water resistance to phase assemblage, pore structure, interfacial characteristics, and water-induced degradation.

The SEM micrographs of MOS cement subjected to 56 days of water curing are shown in Fig. 12. Flat-like and flower-like crystals were observed in the MOSAH1 matrix. According to EDS results (Points 1, 2 and 3), these crystals exhibited an elemental composition similar to that of the 5·1·7 phase (see Fig. 12 (a)). In addition, the sulfur content indicated that the observed crystals were neither $Mg(OH)_2$ nor MgO. In Fig. 12(b), the distribution of Mg, O, and S in the flat-like crystal located at the pore edge was similar to that of the

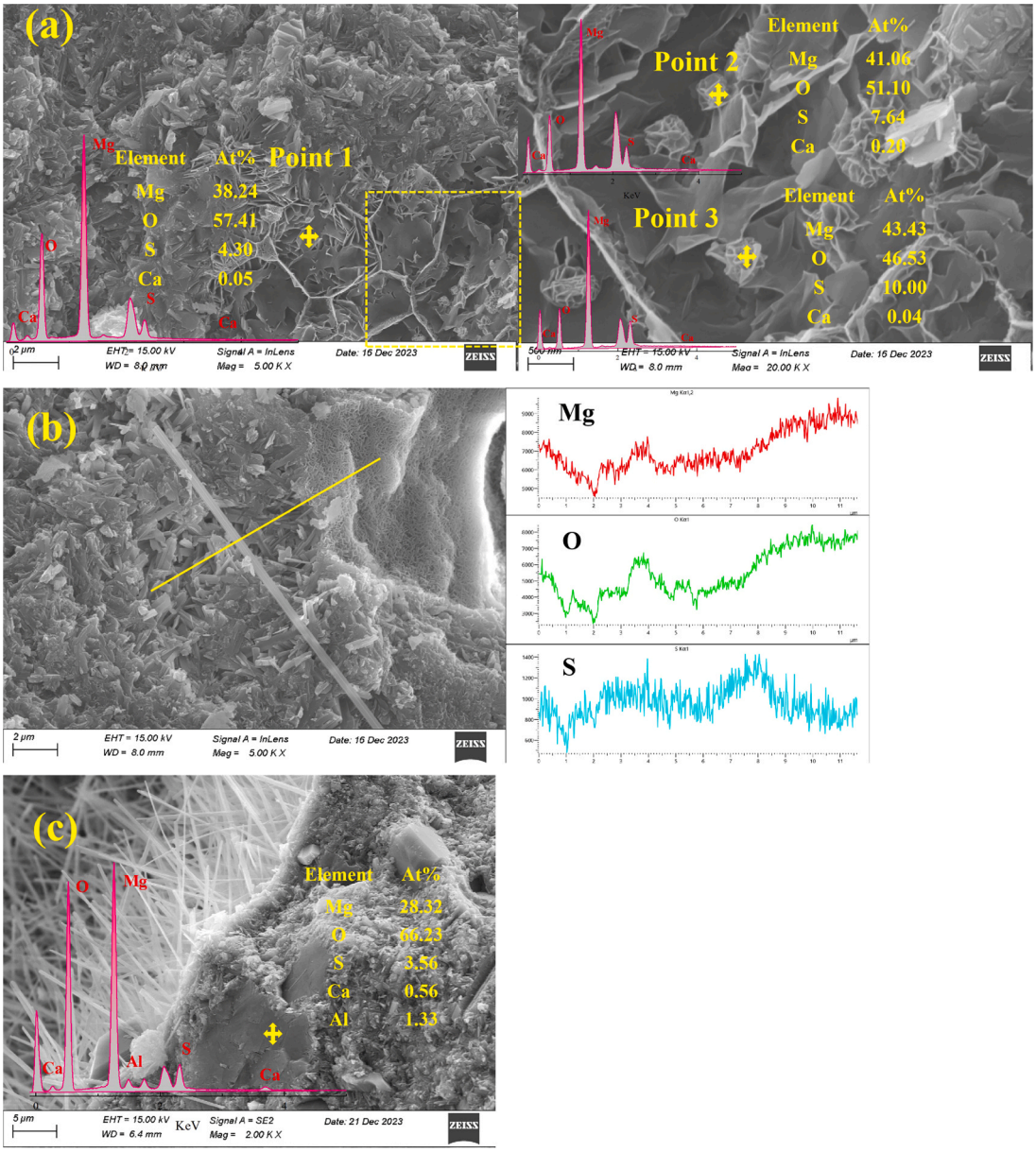

Fig. 12. SEM images of MOS cement: (a), (b) MOSAH1; (c) MOSAH3.

detected 5·1·7 phase. In general, the 5·1·7 phase is needle-like in morphology, while the flat-like and flower-like crystals observed here differed from the typical morphology of the 5·1·7 phase. The post-immersion TG-DTG results indicate substantial changes in the low-temperature dehydration behaviour of the MOS cement, particularly the marked weakening of the peak near 90 °C associated with crystal-water loss from the 5·1·7 phase. This provides evidence that the 5·1·7 phase underwent partial destabilisation or transformation during water immersion. The flat-like and flower-like crystals observed by SEM contained Mg, O, and S and differed morphologically from the typical needle-like 5·1·7 phase. Their morphology showed some similarity to previously reported 3·1·8 crystals [38]. When comparing the DTG traces in Fig. 5 and Fig. 11(b) for 5·1·7 phase decomposition within 45–200 °C, the peak at approximately 90 °C was found to be substantially reduced after immersion, to the point of being barely discernible. The DTG curve changes indicate that a portion of crystal water was released from the 5·1·7 phase during water immersion, as summarised in Reaction (3):

$$5Mg(OH)_2{\cdot}MgSO_4{\cdot}7H_2O \rightarrow aMg(OH)_2{\cdot}bMgSO_4{\cdot}cH_2O + dH_2O \quad (3)$$

These observations suggest that the flat and flower-like crystalline formations were intimately connected to the partial dissolution of the 5·1·7 phase following water exposure. In Fig. 12(c), the observed feature resembled that shown in Fig. 9(c), where a certain amount of Al was present on the matrix surface, suggesting that amorphous aluminium hydroxide remained in the matrix after water immersion. Beyond improving the water resistance of MOS cement, this finding verified that the Al detected on the surface of the MOS cement matrix was present by design rather than by chance

4. Mechanistic role of $Al(OH)_3$ in the hydration, microstructure and performance development of MOS cement

$Al(OH)_3$ was an amphoteric hydroxide that can react with both acids and alkalis. It exists in several crystalline forms, including amorphous aluminium hydroxide, gibbsite, bayerite, boehmite, and others [37,39]. Based on Figs. 1 and 2, the $Al(OH)_3$ used in this study was identified as gibbsite. Owing to its characteristics, $Al(OH)_3$ was able to participate in the MgO hydration reaction. The nucleation and growth of strength phases within MOS cement are driven by MgO hydration and accompanied by changes in the alkalinity of the pore solution. The primary hydration reactions occurring in the MOS cement system are summarised by Reactions (4) and (5) [40]. The hydration behaviour of MOS cement was critically governed by CA, which hindered $Mg(OH)_2$ precipitation and enhanced 5·1·7 phase crystallisation through complexation. Crystal size calculations based on Fig. 4 revealed that the addition of $Al(OH)_3$ suppressed the growth of $Mg(OH)_2$ crystals while increasing the crystal size of the 5·1·7 phase. The results, presented in Fig. S2, show that the pH value decreased with increasing $Al(OH)_3$ dosage. This supports the proposed mechanism that $Al(OH)_3$ interacts with OH^- in the MOS cement system, thereby altering the alkalinity of the pore solution and influencing the formation and growth of hydration products. Since the same amount of CA was used in all mixtures, these changes cannot be attributed to CA alone. Considering the data in Figs. 9–11, which demonstrates the generation of amorphous aluminium hydroxide, $Al(OH)_3$ can be inferred to have directly participated in the hydration reactions. Changes in the 5·1·7 phase and $Mg(OH)_2$ contents shown in Fig. 5 provide further support for this interpretation. Hydration of MgO begins at its surface and is accompanied by the release of OH^-. CA attached to the hydrated MgO surface and acted as a multidentate ligand for metal ions, thereby accelerating the self-organisation of SO_4^{2-}, OH^-, and other constituents into the 5·1·7 phase [9,41]. OH^- is involved in the formation of hydration products. Consequently, changes in pore solution alkalinity begin as soon as MgO hydration starts. The dissolution of gibbsite is mainly driven by alkalinity, and its reaction with OH^- leads to the existence of $Al(OH)_4^-$[42,43]. The consumption of OH^- affects hydration product formation and suppresses the rapid rise in alkalinity. Because strength phases require OH^- for their formation, this mechanism explains the reduction in the contents of these phases observed in the TG-DTG curves.

$$MgO + H_2O \rightarrow MgOH^+_{(surface)} + OH^- \rightarrow MgOH^+ \cdot OH^-_{(surface)} \rightarrow Mg(OH)_2 \quad (4)$$

$$MgO + H_2O + MgSO_4 \rightarrow 5Mg(OH)_2 \cdot MgSO_4 \cdot 7H_2O \quad (5)$$

The concentration of OH^- is closely correlated to the generation of $Mg(OH)_2$[28,29]. Consumption of OH^- hinders the nucleation of $Mg(OH)_2$ crystals and limits the increase in $Mg(OH)_2$ content. By hindering $Mg(OH)_2$ precipitation, the system fosters the development of the 5·1·7 crystalline phase. In this respect, $Al(OH)_3$ plays a role similar to that of CA, although its effect is weaker. The change in OH^- concentration promotes the growth of the 5·1·7 crystal size but inhibits an increase in its total content, while still benefiting the MOS cement's mechanical properties development. Although the 5·1·7 phase is essential in the strength evolution process, the introduction of $Al(OH)_3$ also induces the generation of amorphous aluminium hydroxide, which modifies the crystal size of the hydration products and partly compensates for the negative effects associated with the reduced 5·1·7 phase content. The increase in pores, smaller than 10 nm in Fig. 7, gives indirect evidence of this effect caused by the $Al(OH)_3$. Given that saturated $Mg(OH)_2$ at 298.2 K reaches a pH of approximately 10.73 [44], it is this hydroxide that principally determines the pore solution pH of MOS cement. While $Al(OH)_3$ is present and the pH value exceeds 10, $Al(OH)_4^-$ becomes the predominant dissolved aluminium species [44]. However, complete dissolution of $Al(OH)_3$ generally requires a pH above 13, which explains why residual $Al(OH)_3$ crystals were still observed within the matrix (Fig. 9). Formation of $Al(OH)_4^-$ may be the basis for boehmite growth, which typically occurs within a pH range of 8–10 [39]. Since the pore solution pH of MOS cement decreases to 9.15 after 28 days of curing [29], this falls within the range favourable for boehmite formation. Nevertheless, the results in Fig. 10 do not provide direct evidence for boehmite. Instead, the AlO_5 pentahedral and AlO_4 tetrahedral coordination observed in the ^{27}Al NMR spectra support the formation of amorphous aluminium hydroxide. This is likely related to the encapsulation effect of amorphous aluminium hydroxide, the relatively low pore solution pH of MOS cement, and the relatively low concentration of dissolved Al^{3+}[45,46].

Previous studies [6,9] have shown that CA promotes the formation of the 5·1·7 phase through complexation with Mg-bearing species and regulation of the interfacial assembly of Mg^{2+}, OH^-, and SO_4^{2-} during MgO hydration. In contrast, $Al(OH)_3$ participates in the evolving alkaline pore-solution environment through its amphoteric reactivity and can consume OH^- through the formation of soluble aluminate species. Therefore, the effects of CA and $Al(OH)_3$ are neither purely synergistic nor purely competitive; rather, their interaction is dosage-dependent. At an appropriate $Al(OH)_3$ dosage, partial regulation of the OH^- environment suppresses excessive $Mg(OH)_2$ formation and modifies the crystalline development of the 5·1·7 phase, while the formation of amorphous aluminium-bearing species and the associated microstructural densification compensate for, or outweigh, the reduction in the amount of the 5·1·7 phase. This produces a net beneficial effect on mechanical properties and water resistance. At excessive $Al(OH)_3$ dosage, however, stronger perturbation of the OH^- environment may overly suppress the formation of the 5·1·7 phase. At the same time, the larger amount of residual crystalline $Al(OH)_3$ may not contribute effectively to load-bearing hydrate formation and could introduce heterogeneous or

mechanically weak regions within the matrix. Under these conditions, the beneficial effects of amorphous aluminium-bearing species and pore refinement are insufficient to compensate for the loss of the principal strength-contributing 5·1·7 phase, resulting in reduced strength.

After water immersion, amorphous aluminium hydroxide was still observed in the matrix (Fig. 12), although NMR results indicated a reduction in its content, possibly owing to the dissolution of $Al(OH)_4^-$. At the same time, the TG results presented in Fig. 11 suggest that $Al(OH)_3$ restrained the generation of extra hydration products throughout water exposure, thereby partially offsetting the adverse effect of residual MgO hydration. The above phenomenon provides a partial explanation for the better water resistance achieved in $Al(OH)_3$-containing MOS cement. Besides, the significant difference in the 5·1·7 phase decomposition peaks, attributed to the loss of crystal water during temperature rise process (Fig. 5 and Fig. 11(b)), indicated that the 5·1·7 phase was unstable in water, which was closely associated with the presence of flat-like or flower-like crystals observed in Fig. 12. The participation of $Al(OH)_3$ in MOS cement hydration led to superior mechanical behaviour and improved water resistance.

At 3% $Al(OH)_3$, MOSAH2 exhibited the lowest total porosity and smallest average pore size, providing the most favourable compact matrix for compressive load bearing and resulting in the highest 28-d compressive strength. Increasing the $Al(OH)_3$ dosage to 6% slightly increased total porosity relative to MOSAH2 but produced the largest fraction of pores smaller than 10 nm and maintained a substantially lower fraction of pores larger than 100 nm than the control. Meanwhile, the characterisation results indicated increased involvement of amorphous aluminium-bearing species and their close association with the 5·1·7 phase. These features may be more beneficial to flexural performance, which is sensitive to local defects and interfacial continuity, and to water resistance, which depends on resistance to water ingress and water-induced degradation of the 5·1·7 phase. Therefore, the dosage shift reflects a balance among matrix compactness, pore-size distribution, 5·1·7 phase evolution, and amorphous aluminium-bearing phase formation. A lower $Al(OH)_3$ dosage was optimal for compressive strength because it produced the densest overall matrix, whereas the 6% dosage provided a more favourable combination of fine-pore development and water-resistant interfacial characteristics.

Overall, $Al(OH)_3$ affects MOS cement in several interconnected ways: it participates in hydration by consuming OH^-, inhibiting $Mg(OH)_2$ crystallisation, modulating 5·1·7 phase growth, and fostering amorphous aluminium hydroxide formation. Changes in the growth of the 5·1·7 phase and $Mg(OH)_2$ reinforce the conclusion that $Al(OH)_3$ was actively involved in MOS cement hydration. These combined effects result in a denser microstructure, characterised by reduced porosity and smaller pore sizes, thereby enhancing both compressive and flexural strength. Although the 5·1·7 phase plays a key role in the development of mechanical properties, the variations in its content and crystal size (Figs. 4 and 5) provide clear evidence of the positive influence of $Al(OH)_3$ on the engineering performance of MOS cement. In addition, amorphous aluminium hydroxide appears to be interwoven with, or adsorbed onto, the 5·1·7 phase, which may reduce the susceptibility of this phase to water erosion. The improved water resistance of MOS cement, together with the microstructural features observed in SEM images, highlights the beneficial role of amorphous aluminium hydroxide within the matrix. Furthermore, the relatively insoluble nature of amorphous aluminium hydroxide helps to mitigate the detrimental effects associated with residual MgO hydration and the resulting volume instability under wet conditions. Therefore, $Al(OH)_3$ enhances both the mechanical properties and water resistance of MOS cement through coupled effects on hydration chemistry, phase evolution, and microstructural densification. The strength development of MOS cement was primarily governed by the composition and evolution of its hydration products. The characterisation results confirmed that $Al(OH)_3$ participated in the hydration process and promoted the formation of amorphous aluminium hydroxide (Fig. 8). However, this process simultaneously altered the formation of the 5·1·7 phase (Fig. 5), which is the principal strength-bearing phase in MOS cement. Changes in the gel-pore fraction partially reflected the evolution of gel-like products within the matrix. Increasing the $Al(OH)_3$ dosage promoted gel formation and was associated with an increased contribution of amorphous aluminium hydroxide. Nevertheless, the mechanical performance was governed by the overall pore structure rather than the gel-pore fraction alone. Although MOSAH3 exhibited an increased gel-pore fraction, the concurrent increase in pores larger than 100 nm resulted in a lower compressive strength than that of MOSAH2 (Fig. 7). Furthermore, the DTG results after water immersion (Fig. 11(b)), together with the HR-TEM observations (Fig. 10), suggested that amorphous aluminium hydroxide interwoven with or deposited on the 5·1·7 phase provided a protective effect against water-induced deterioration. This effect contributed to the improved water resistance of $Al(OH)_3$-modified MOS cement.

A schematic diagram (Fig. 13) was proposed to provide a clearer and more insightful description of the proposed mechanism of how $Al(OH)_3$ influences the hydration, microstructure and performance development of MOS cement which illustrates the proposed causal chain linking: (i) MgO hydration and OH^- release; (ii) the interaction of $Al(OH)_3$ with the evolving alkaline pore solution; (iii) OH^- consumption and changes in local aluminium speciation; (iv) suppression of $Mg(OH)_2$ formation and crystalline growth; (v) regulation of the formation and crystalline development of the 5·1·7 phase; (vi) formation and interfacial distribution of amorphous aluminium-bearing species; and (vii) subsequent pore refinement and matrix densification. As schematically illustrated in Fig. 13, the modification mechanism of $Al(OH)_3$ differs from those reported for fly ash and magnesium slag [27,47]. $Al(OH)_3$ consumed OH^- released during MgO hydration, thereby buffering the increase in pore-solution alkalinity and suppressing the formation and crystal growth of $Mg(OH)_2$. Meanwhile, the altered OH^- availability regulated the formation and crystal growth of the 5·1·7 phase and promoted the formation of amorphous aluminium hydroxide. These coupled effects modified the hydration-product assemblage and pore structure, ultimately governing the mechanical properties and water resistance of MOS cement. Previous studies have demonstrated that the 5·1·7 phase is unstable under highly alkaline conditions [48]. Therefore, the pH-regulating effect of $Al(OH)_3$ may provide a potential strategy for improving the environmental adaptability of MOS cement, particularly for applications involving alkaline exposure. Further investigation under simulated saline–alkali exposure conditions is required to verify this potential.

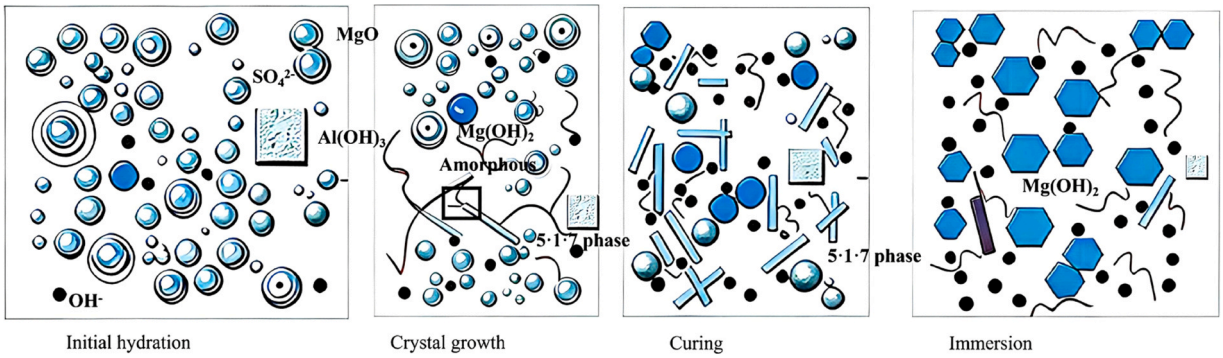

Fig. 13. Schematic diagram of property evolution of MOS cement modified by $Al(OH)_3$.

5. Conclusions

This study focused on the effects of $Al(OH)_3$ on MOS cement, covering both mechanical properties and water resistance, and delved into the underlying mechanisms through which $Al(OH)_3$ engages in hydration and shapes the development of hydration products and strength. The outcomes contribute novel understanding regarding the use of additives to boost the strength and application of MOS cement. The principal conclusions are outlined below:

1. The MOS cement mixture with 3% $Al(OH)_3$ outperformed all others, delivering a compressive strength of 81.6 MPa at 28 days of air curing. At a 6% $Al(OH)_3$ dosage, the flexural strength attained 21.5 MPa, marking a 37.8% improvement over the control specimen. Following 56 days of water immersion, the MOS cement with 6% $Al(OH)_3$ delivered the maximum compressive strength of 59.1 MPa. The data suggest that an optimal dosage of $Al(OH)_3$ effectively boosts both the strength and water resistance of MOS cement.

2. As MOS cement hydrated, the incorporated $Al(OH)_3$ generated amorphous aluminium hydroxide that coated the matrix and became intimately interwoven with the 5·1·7 phase. $Al(OH)_3$ inhibited the growth of $Mg(OH)_2$ crystals while promoting the growth of the 5·1·7 phase through its participation in the hydration. A rise in the proportion of pores below 10 nm also suggested that $Al(OH)_3$ contributed to matrix densification in MOS cement.

3. After exposure to water, the MOS cement matrix exhibited tabular and flower-like crystals, which were confirmed to be basic magnesium sulfate whiskers. These crystals differed morphologically from the 5·1·7 phase and were closely associated with water exposure, during which the metastability of the 5·1·7 phase triggered the release of crystal water and alterations in hydration product content. In particular, the evolution of the 5·1·7 phase highlighted the positive role of amorphous aluminium hydroxide in mitigating water-induced deterioration and promoting the retention of MOS cement properties.

4. The enhancement mechanism of $Al(OH)_3$ in MOS cement is governed by its regulation of the hydration process. Specifically, $Al(OH)_3$ participates in hydration by consuming OH^-, which alters the balance between $Mg(OH)_2$ formation and 5·1·7 phase development. This chemical regulation, together with the formation of amorphous aluminium hydroxide, provides a coupled effect of hydration control and microstructural stabilisation. As a result, the improved mechanical performance and water resistance of MOS cement arise from a synergistic interplay among ion regulation, phase evolution, and matrix stabilisation, rather than from a single dominant factor.

CRediT authorship contribution statement

Xiangming Zhou: Writing – review & editing, Validation, Supervision, Resources, Project administration, Methodology, Investigation, Funding acquisition, Conceptualization. **Wei Wang:** Methodology, Investigation, Data curation. **Hailong Wang:** Validation, Supervision, Resources, Project administration, Methodology, Funding acquisition, Data curation, Conceptualization. **Zhiqi Hu:** Methodology, Formal analysis, Data curation. **Huijun Xue:** Investigation, Formal analysis, Data curation. **Kairong Jin:** Writing – original draft, Visualization, Validation, Methodology, Investigation, Formal analysis, Data curation.

Declaration of Competing Interest

The authors declare that they have no known competing financial interests or personal relationships that could have appeared to influence the work reported in this paper.

Acknowledgements

The authors would like to thank the financial support from the 2025 Science and Technology Support Project of State Key Laboratory of Water Engineering Ecology and Environment in Arid Area (2025GJCXPT01014), the National Natural Science Foundation of China (52469024, 52469023, 52569024), Natural Science Foundation of Inner Mongolia Autonomous Region (2026QC0604,

NDYB2025–96, 2024MS05054), Research on Activation and Strengthening Technology of Ecological Negative Carbon Aggregates Based on Coal Mine Powder Slag (ST2024005), and the UK Research & Innovation (EP/X04145X/1, i.e., the CSTO2NE project).

Appendix A. Supporting information

Supplementary data associated with this article can be found in the online version at doi:10.1016/j.cscm.2026.e06407.

Data availability

Data will be made available on request.

References

[1] P.J.M. Monteiro, S.A. Miller, A.D. Horvath, Produce and use with care, Nat. Mater. 16 (7) (2017).
[2] S.A. Walling, J.L. Provis, Magnesia-based cements: a journey of 150 years, and cements for the future? Chem. Rev. 116 (7) (2016).
[3] H. Fu, R. Mo, P.G. Wang, Y.R. Wang, Y.B. Cao, W.T. Guang, Y. Ding, Influence of elevated temperatures and cooling method on the microstructure development and phase evolution of alkali-activated slag, Materials 15 (6) (2022).
[4] S. Shi, H. Li, Q.Z. Zhou, H.Z. Zhang, P.A.M. Basheer, Y. Bai, Alkali-activated fly ash cured with pulsed microwave and thermal oven: A comparison of reaction products, microstructure and compressive strength, Cem. Concr. Res. 166 (2023).
[5] H.M. Zhu, H. Li, X.D. Ma, F. Wu, Q.Z. Zhou, Y. Bai, Combined effect of coal chemical wastewater and PC on preparing of coal-to-liquids residue-based alkali activated materials, J. Hazard. Mater. 405 (2021).
[6] X.Y. Chen, S.Y. Wang, Y.X. Zhou, C. Cheeseman, W.L. Bi, T.T. Zhang, Improved low-carbon magnesium oxysulfate cement pastes containing boric acid and citric acid, Cem. Concr. Compos. 134 (134) (2022).
[7] D.A. Kellen, G.C. Marmorato, Behaviour of autoclaved magnesium oxysulfate cement pastes, J. Build. Eng. 76 (76) (2023).
[8] R.E. Dinnebier, M. Pannach, D. Freyer, 3Mg(OH)2·MgSO4·8H2O: A Metastable Phase in the System Mg(OH)2-MgSO4-H2O, Z. F. üR. Anorg. und Allg. Chem. 639 (10) (2013).
[9] N. Wang, H.F. Yu, W.L. Bi, Y.S. Tan, N. Zhang, C.Y. Wu, H.Y. Ma, S. Hua, Effects of sodium citrate and citric acid on the properties of magnesium oxysulfate cement, Constr. Build. Mater. 169 (169) (2018).
[10] C.Y. Wu, W.H. Chen, H.F. Zhang, H.F. Yu, W.Y. Zhang, N.S. Jiang, L.X. Liu, The Hydration Mechanism and Performance of Modified Magnesium Oxysulfate Cement by Tartaric Acid, Constr. Build. Mater. 144 (144) (2017).
[11] N. Zhang, W.J. Feng, Y. Su, H.F. Yu, M.F. Ba, Z.M. He, Different effects for phosphoric acid and calcium citrate on properties of magnesium oxysulfate cement, Constr. Build. Mater. 374 (374) (2023).
[12] X.Y. Chen, T.T. Zhang, C. Cheeseman, W.L. Bi, S.Y. Wang, Production of Rapid-Hardening Magnesium Oxysulfate Cement Containing Boric Acid, J. Mater. Civil. Eng. 34 (5) (2022).
[13] N. Zhang, H.F. Yu, H.Y. Ma, Y.T. Diao, T. Liu, C.Y. Wu, Effect of Ammonium Citrate Tribasic on the Hydration Reaction and Properties of Magnesium Oxysulfate Cement, J. Mater. Civil. Eng. 33 (11) (2021).
[14] T. Guo, H.F. Wang, H.J. Yang, X.S. Cai, Q. Ma, S.M. Yang, The mechanical properties of magnesium oxysulfate cement enhanced with 517 phase magnesium oxysulfate whiskers, Constr. Build. Mater. 150 (150) (2017).
[15] L. Qin, X.J. Gao, W.G. Li, H. Ye, Modification of Magnesium Oxysulfate Cement by Incorporating Weak Acids, J. Mater. Civil. Eng. 30 (9) (2018).
[16] X.Y. Chen, B. Chen, J. Chang, X.X. Xu, E.Y. Sun, S.Y. Wang, Y. Guan, Improved mechanical strength of magnesium oxysulfate cement using ferric sulfate, J. Build. Eng. 67 (67) (2023).
[17] K.R. Jin, W.L. Bi, Y. Guan, X.Y. Chen, X.M. Zhou, D.Z. Wang, Performance of magnesium oxysulfate (MOS) cement with granite powders after combined sulfate and chloride attacks, Constr. Build. Mater. 366 (366) (2023).
[18] Y.S. Tan, H.F. Yu, S.K. Sun, C.Y. Wu, H. Ding, Properties and microstructure of basic magnesium sulfate cement: Influence of silica fume, Constr. Build. Mater. 266 (2021).
[19] Q.Y. Li, L.C. Zhang, X.J. Gao, J.Y. Zhang, Effect of pulverized fuel ash, ground granulated blast-furnace slag and CO2 curing on performance of magnesium oxysulfate cement, Constr. Build. Mater. 230 (C) (2020).
[20] K. Gu, B. Chen, H.F. Yu, N. Zhang, W.L. Bi, Y. Guan, Characterization of magnesium-calcium oxysulfate cement prepared by replacing MgSO4 in magnesium oxysulfate cement with untreated desulfurization gypsum, Cem. Concr. Compos. (2021).
[21] Y. Guan, Z.Q. Hu, Z.H. Zhang, J. Chang, W.L. Bi, C. Cheeseman, T.T. Zhang, Effect of hydromagnesite addition on the properties and water resistance of magnesium oxysulfate (MOS) cement, Cem. Concr. Res. 143 (143) (2021).
[22] G. Ovcharenko, E. Ibe, The role of aluminum and iron hydroxides in the formation of concrete properties, IOP Conference Series Materials Science Engineering 1030 (1) (2021).
[23] J. Chang, Y.Y. Zhang, X.P. Shang, J.Y. Zhao, X. Yu, Effects of amorphous AH3 phase on mechanical properties and hydration process of C4A3S-CSH2-CH-H2O system, Constr. Build. Mater. 133 (133) (2017).
[24] Y.Y. Zhang, J. Chang, J. Ji, AH3 phase in the hydration product system of AFt-AFm-AH3 in calcium sulfoaluminate cements: A microstructural study, Constr. Build. Mater. 167 (167) (2018).
[25] J. Goergens, R. Belli, C. Schulbert, F.G. Neunhoeffer, Influence of different CA2/CA-ratios on hydration degree, AH3 content and flexural strength investigated for a binder formulation of calcium aluminate cement with calcite, Cem. Concr. Res. 165 (165) (2023).
[26] S.W. Tang, C.R. Wei, R.J. Cai, J.S. Huang, E. Chen, J.H. Yuan, situ monitoring of pore structure of magnesium oxysulfate cement paste: Effect of $MgSO_4/H_2O$ ratio, J. Ind. Eng. Chem. 83 (2020) 387–400.
[27] N. Zhang, H.F. Yu, W. Gong, T. Liu, N. Wang, Y.S. Tan, C.Y. Wu, Effects of low- and high-calcium fly ash on the water resistance of magnesium oxysulfate cement, Constr. Build. Mater. 230 (2020) 116951.
[28] K.R. Jin, C.J. Wu, Z.M. Xiong, D.Z. Wang, X.M. Zhou, X.Y. Chen, Impact of Cl- on the performance of magnesium oxysulfate (MOS) cement, Constr. Build. Mater. 430 (2024) 136472.
[29] T.T. Zhang, J.B. Zhang, J. Chang, W.L. Bi, C. Cheeseman, X.Y. Chen, Hydration and strength development in magnesium oxysulfate (MOS) cement incorporating silicic acid, Compos. Part. B 268 (2024).
[30] Z.Q. Hu, J. Chang, X.Y. Chen, Y. Guan, W.L. Bi, Preparation of magnesium oxysulfate cement with semidry carbonation high calcium content light-burned magnesium (Ca-LBM), Constr. Build. Mater. 408 (2023).
[31] J. Chang, Z.Q. Hu, W.L. Bi, Y. Guan, Mechanism of CaO in Light-Burned Magnesia on the Formation Process, Mechanical Properties, and Water and Chloride Resistance of the 517 Phase, J. Mater. Civil. Eng. 35 (6) (2023).
[32] D. Wang, J. Chang, W.S. Ansari, The effects of carbonation and hydration on the mineralogy and microstructure of basic oxygen furnace slag products, J. CO2 Util. (2019) 3487–3498.

[33] J.R. Shan, B.W. Yang, Y.Q. Su, G.H. Chong, L.Q.C. Abdullah, X.H. Qi, H.X. Guo, Microwave irradiation-assisted isomerization of glucose to fructose over Mg/Al-doped lignin self-assembled nanospheres, Appl. Catal. B Environ. Energy 379 (2025) 125682.
[34] T. Meher, A.K. Basu, S. Ghatak, Physicochemical characteristics of alumina gel in hydroxyhydrogel and normal form, Ceram. Int. 31 (6) (2004) 831–838.
[35] P. Padmaja, G.M. Anilkumar, P. Mukundan, G. Aruldhas, K.G.K. Warrier, Characterisation of stoichiometric sol–gel mullite by fourier transform infrared spectroscopy, Int. J. Inorg. Mater. 3 (7) (2001) 693–698.
[36] T.T. Zhang, Q. Guo, X.Q. Chen, C. Cheeseman, H. Wang, J. Chang, Unlocking the role of silica gel in enhancing mechanical properties and water resistance of magnesium oxysulfate cement, Cem. Concr. Compos. 157 (2025) 105941.
[37] T. Isobe, T. Watanabe, J.B.E. Caillerie, A.P. Legrand, D. Massiot, Solid-state 1H and 27Al NMR studies of amorphous aluminum hydroxides, J. Colloid Interface Sci. 261 (2) (2003) 320–324.
[38] N. Zhang, H.F. Yu, H.Y. Ma, H.X. Ma, M.F. Ba, The phase composition of the MgO-MgSO4-H2O system and mechanisms of chemical additives, Compos. Part. B 247 (2022).
[39] A. Kocjan, A. Dakskobler, T. Kosma, Evolution of aluminum hydroxides in diluted aqueous aluminum nitride powder suspensions, Cryst. Growth & Des. 12 (3) (2012) 1299–1307.
[40] L.F. Amaral, I.R. Oliveira, R. Salomão, E. Frollini, V.C. Pandolfelli, Temperature and common-ion effect on magnesium oxide (MgO) hydration, Ceram. Int. 36 (3) (2009) 1047–1054.
[41] Z.H. Zhou, Y.F. Deng, H.L. Wan, Structural diversities of cobalt(II) coordination polymers with citric acid, Cryst. Growth & Des. 5 (3) (2005) 1109–1117.
[42] H.M. May, P.A. Helmke, M.L. Jackson, Gibbsite solubility and thermodynamic properties of hydroxy-aluminum ions in aqueous solution at 25 °C, Geochim. Et. Cosmochim. Acta 43 (6) (1979) 861–868.
[43] E.H. Wang, J.H. Chen, X.J. Hu, K.C. Chou, X.M. Hou, Evolution of aluminum hydroxides at the initial stage of aluminum nitride powder hydrolysis, Ceram. Int. 42 (9) (2016) 11429–11434.
[44] W.C. Gao, Z.B. Li, Solubility and KSP of $Mg_4Al_2(OH)_{14}{\cdot}3H_2O$ at the various ionic strengths, Hydrometallurgy 117 (2012).
[45] Y.Y. Zhang, Q.X. Zhao, Z.M. Gao, J. Chang, Nanostructural evolution of Al(OH)3 gel formed by the cubic and orthorhombic ye'elimite clinkers of calcium sulfoaluminate cements in an ultra-wide hydration temperature range, Cem. Concr. Res. 150 (2021) 106607.
[46] J.C. Li, T. Zeng, J. Chang, Nanostructure evolution of $(A/F)H_3$ phase with different alkali concentrations based on calcium sulfoaluminate cement, Cem. Concr. Res. 172 (2023).
[47] D.Z. Wang, K.R. Jin, N. Wang, H.W. Zhang, J.H. Wang, X.M. Zhou, Compressive strength and water resistance of magnesium oxysulfate (MOS) cement incorporating magnesium slag, Constr. Build. Mater. 453 (2024), 139053-139053.
[48] J.Y. Zhao, J.H. Xu, C.Y. Cui, C.Y. Yu, J. Chang, Z.Q. Hu, W.L. Bi, Stability and phase transition of 5·1·7 phase in alkaline solutions, Constr. Build. Mater. 258 (2020).